

This is a preprint version of the article published in:
Composites Part B: Engineering, Vol. 187 (2020), 107833.
<http://dx.doi.org/10.1016/j.compositesb.2020.107833>

Please, cite this document as:

K. C. OPIELA, T. G. ZIELIŃSKI. "Microstructural design, manufacturing and dual-scale modelling of an adaptable porous composite sound absorber." *Composites Part B: Engineering*, Vol. 187 (2020), 107833.

DOI: [10.1016/j.compositesb.2020.107833](https://doi.org/10.1016/j.compositesb.2020.107833)

Microstructural design, manufacturing and dual-scale modelling of an adaptable porous composite sound absorber

KAMIL C. OPIELA TOMASZ G. ZIELIŃSKI*

Institute of Fundamental Technological Research, Polish Academy of Sciences
ul. Pawińskiego 5B, 02-106 Warsaw, Poland

*Corresponding author, e-mail: tzielins@ippt.pan.pl

Abstract

This work investigates a porous composite with modifiable micro-geometry so that its ability to absorb noise can be accommodated to different frequency ranges. The polymeric skeleton of the composite has a specific periodic structure with two types of pores (larger and smaller ones) and two types of channels (wide and narrow ones), and each of the large pores contains a small steel ball. Depending on the situation, the balls block different channels that connect the pores, and therefore alter the visco-inertial phenomena between the saturating air and solid skeleton which take place at the micro-scale level and are responsible for the dissipation of the energy of acoustic waves penetrating the porous composite. All this is studied numerically using the advanced dual-scale modelling, and the results are verified by the corresponding experimental tests of 3D-printed samples. Particular attention is paid to the prototyping and additive manufacturing of such adaptive porous composites.

Key words: porous composite, adaptive sound absorber, microstructure-based modelling, additive manufacturing.

1 Introduction

Porous sound absorbing or insulating composites are usually developed as enhanced, or simply, specific acoustic treatments. Some of the proposed solutions involve advanced technologies as, for example, in the case of a sound insulation nano-composite based on the epoxy resin with synthesized hollow silica nanotubes as functional fillers [1], while the others are based on more common or typical components, like in the case of a porous composite fabricated by filling a polyurethane foam with sawdust [2], or in the case of a typical composite honeycomb sandwich panel—studied experimentally in [3]—where the increase in sound transmission loss had been achieved by filling the cells with different glass fibre assemblies. Original porous composite solutions based on studies involving more advanced physical insight often lead to meta-porous materials, see for example [4–11]. Finally, in recent years, several types of active or semi-active (adaptive) noise insulating porous composite treatments have been studied [12–20], however, these active/adaptive composite solutions are based on the macro- and meso-scale investigations, that is, with no direct and intentional influence on the micro-geometry of porous media.

The porous composite absorber proposed in this work can adapt to different (specified) noise conditions thanks to possible (controlled) change in its porous microstructure, and the whole design of this composite as well as the predictions of sound absorption are derived from the analyses based on its micro-geometry. Such a microstructure-based approach is now well established. It started with advanced theoretical studies [21–27] of the relation between the visco-thermal phenomena and acoustic wave propagation in various porous, fibrous and granular media [28–31] and their micro-geometry, and more recently, it has resulted in many works involving numerical calculations on more or less complex micro-geometrical domains; in particular, the microstructure-based modelling has been applied for: open-cell aluminium foams [32, 33], perforated closed-cell metallic foams [34], ceramic foams with spherical pores [35], polymeric foams [36–42], double-porosity foams [43], syntactic hybrid foams (i.e., open-cell polyurethane foams with embedded hollow microbeads) [44], 3D-printed foams [45], granular media [46–49] and fibrous materials [50–56], and even micro-perforated plates with complex patterns of micro-slits [57].

In the workflow of present investigation, a demonstrator illustrating the potential behind the whole adaptable microstructure concept was fabricated in the form of a porous composite specimen—with polymeric skeleton and steel balls as movable fillers—thanks to modern additive manufacturing technologies which allow for forming porous samples with a designed micro-geometry, and therefore, become very useful for prototyping and fabrication (and perhaps, in near future, even mass production) of novel noise attenuating materials, with definite microstructure, see for example [45, 55–58]. In fact, the sample skeleton was 3D-printed from a solid fusible filament, while small steel bearing balls were introduced manually into the large pores of its open-cell periodic microstructure during the production process (one for each large pore) in order to let them act as valves closing or opening the channels between the interconnected voids (and the large pores, in particular), and therefore controlling the character of visco-thermal phenomena taking place on the micro-scale level. The viscous flow and thermal dispersion in porous media are heavily associated with

the propagation and attenuation of acoustic waves, and are reflected in the so-called transport parameters. By altering the position of balls trapped inside pores (thanks to the gravity or inertial forces), one can modify the flow and related transport parameters, and in that way, affect the overall sound attenuation capabilities of the composite material. As it will be shown in this paper, the small but weighty steel balls serve very well the purpose of equipping the designed porous material with a simple yet functional adaptation mechanism.

Although the porous composite absorber presented in this work should rather be treated as a concept demonstrator, such adaptable sound absorbers (of similar design) may be applied as specific noise insulation treatments of mechanical devices where the gravity, acceleration or centrifugal forces can be used for the re-location of tiny valve balls inside a material to accommodate its dissipative characteristics to the existing noise conditions. In fact, the predominant frequencies of the noise generated by operating machines (engines) often increase with speed and while accelerating. Usually, it is possible to precisely determine these frequencies (and also magnitudes) for each particular working stage using signal analysers during acoustical measurement tests. Knowing the character of noise at typical working stages, one can devise the acoustic treatment with a specific adaptable micro-geometry (in a way demonstrated in this work), so that the noise at the required frequencies will be perfectly attenuated depending on the current state of an adaptation mechanism (e.g., positioning of valve balls) realised with an extremely simple (if not primitive) semi-active way. It should be noted that the proposed adaptable absorber with steel valve balls can also be operated using an external magnetic field instead of gravity.

The paper thoroughly describes the whole investigation scheme undertaken to develop the porous composite absorber, namely: design, manufacturing, micro-geometric model updating, micro- and macro-scale analyses, and acoustic measurements. The design of a periodic micro-geometry of porous composite is presented in Section 2. Then, the (non-trivial) manufacturing process of the porous composite and other samples (including auxiliary tools) is discussed in Section 3. The microstructure-based calculations are explained in Section 4, while the related macro-scale modelling of wave propagation and absorption is presented in Section 5, where the final results of sound absorption are confronted with the corresponding measurements of the normal-incidence acoustic absorption coefficient for the auxiliary porous samples as well as for the adaptable porous composite in two adaptation states.

2 Design process of periodic microstructure

Figure 1 shows the main stages of the underwent investigation scheme for the periodic micro-geometry of the proposed sound absorbing material. At the beginning, some preliminary consideration was given to develop an initial form of the fluid domain inside a single periodic unit cell (see Figure 1(a)) that reflects the assumptions of functionality being made. This unitary region efficiently describes the periodic porosity of the sound absorber, which consists of a large number of representative porous solid cells (see Figure 1(b)) arranged into three-dimensional structures (see Figure 1(c)). In that way CAD models of the absorber samples (com-

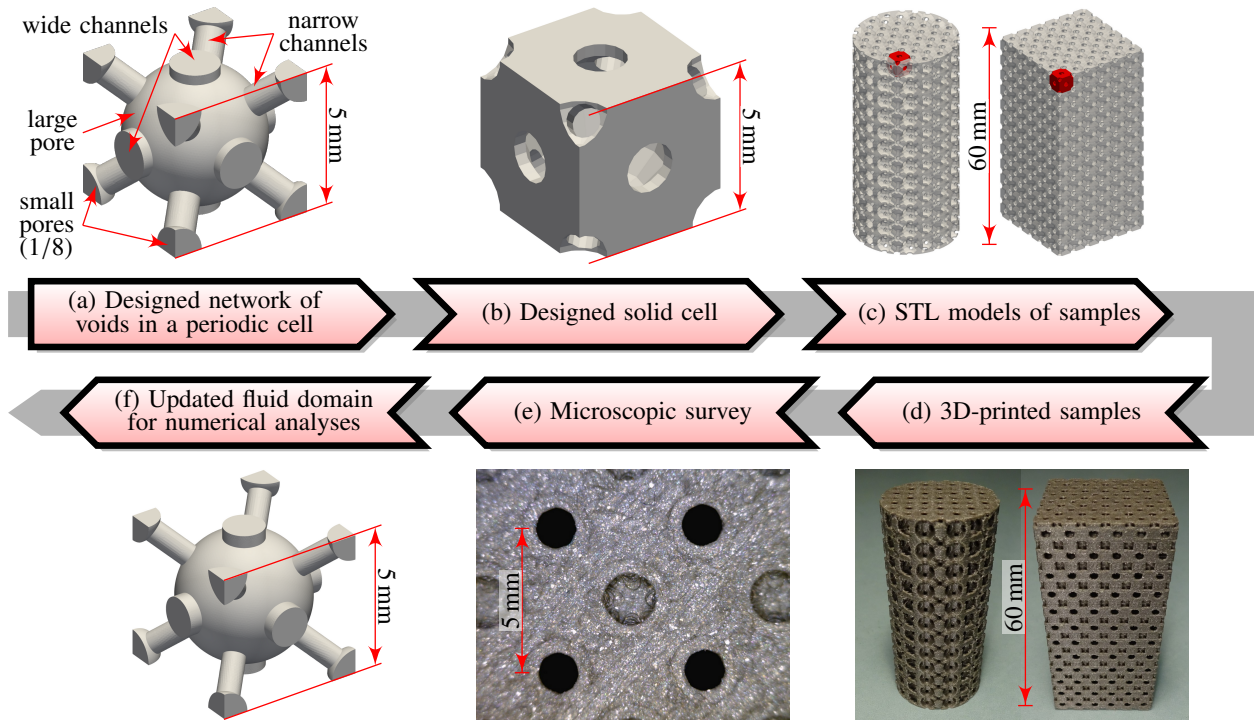


Figure 1: Design and investigation scheme for the composite microstructure: (a) a designed network of voids in a single periodic cell; (b) the corresponding solid cell; (c) the periodic arrangement of cells inside the material CAD models used for 3D printing (a single periodic cell is marked in red); (d) the samples fabricated by additive manufacturing; (e) a microscopic survey of the fabricated specimens (actual dimensions, shapes, etc.); (f) the updated geometry of fluid domain (roughly, the actual network of voids) in the periodic unit cell used for calculations.

posed of many identical individual cells) are formed, and then, such solid skeletons are 3D-printed (see Figure 1(d)) and measured under a microscope (see Figure 1(e)). The results of the microscope survey allow to update the actual micro-geometric dimensions (see Figure 1(f)) for the purposes of further numerical evaluation of various acoustical characteristics of the actual absorber.

The initial (i.e., used for fabrication) as well as the final (i.e., updated and used for final computations) geometries of porous representative cell are cubic and their periodic networks of voids contain (see Figure 1(a,f)):

- a single (major) large pore in the cell centre,
- eight one-eighths of small pores in the cell corners,
- six wide cylindrical channels (two vertical and four horizontal ones) to link the large pore with its counterparts in the neighbouring cells,
- eight oblique narrow cylindrical channels linking the large central pore with the small corner ones.

In the case of the adaptable absorber, the large pore will contain a small steel ball which may block the entry to one of the channels. Obviously, the presence (and position) of such ball will change the volume (and shape) of the fluid domain and the overall porosity of the periodic cell.

The porous cubic cell is obviously scalable. The budget 3D-printing technology utilized for this research permitted only for fabrication of samples with large cells of 5 mm in size. Table 1 shows the diameter values for pores and channels in the cell of such a size, and also the assumed ratio of the diameters with respect to the cell size. The designed porosity of periodic cell is 52%

for the case without ball, however, this value must be verified and updated for the actual (i.e., imperfect) samples 3D-printed from this design. In the case of the adaptable absorbing material, a steel ball of diameter 2.5 mm (which is half of the cell size and 0.543 of the diameter of the large pores) will be inserted inside the major pore of each cell, which means that the designed porosity will decrease in this case to less than 46%.

Table 1: Diameters of pores and channels in the porous periodic cube of size 5 mm used for 3D printing (the middle column shows the ratio of the diameters to the cell-size).

Void type	diameter cell size	Diameter [mm]
large pore	0.92	4.6
small pore	0.36	2.0
wide channel	0.32	1.6
narrow channel	0.20	1.0

3 Manufacturing of the adaptable composite sound absorber

3.1 Additive manufacturing technology

This section deals with the fabrication of porous specimens of the adaptable sound absorber by means of one of the additive manufacturing technologies commonly known as 3D-printing [59, 60]. In principle, these techniques rely on the fact that the layers of material can be successively formed on top of each other and fused together, eventually leading to the final product, which can be used

in many branches of industry. The approach is also very good for high-precision prototyping of customised and complex geometries. There is the whole gamut of allowable substances, including metals, polymers, ceramics and concrete, that one can take advantage of while planning the functional as well as aesthetic characteristics of the output. Among many methods of additive manufacturing such as stereolithography, powder bed fusion, or selective laser sintering, the fused deposition modelling (FDM) is relatively simple-to-use, fast and not very expensive [60]. A comprehensive review of the available options is provided, for instance, in [59–61].

Within the framework of this paper, the FDM printing technology [60] was used. In a nutshell, it is based on heating a continuous filament made of a thermoplastic polymer to the melting temperature at the nozzle, and extruding it either onto the platform or on top of an already existing object. After printing, when the ambient air cools down to room temperature, the entire layer-by-layer structure solidifies and develops its mechanical properties. In fact, the main and most popular materials employed by the technique are polylactic acid (PLA) and acrylonitrile butadiene styrene (ABS). The former needs lower printing temperature and is better suited for designs with fine details, albeit mechanically poor. By contrast, the latter is often preferred when function is more crucial than form, and has great post-processing capabilities in, e.g., surface polishing, sanding [62].

3.2 Porous samples and a porous composite specimen

Two porous samples and one porous composite specimen (see Figure 2) were manufactured using the FDM technology [60], namely: (S-1) a non-adaptable cylindrical porous sample, see Figure 2(a); (S-2) a non-adaptable cuboidal porous sample, see Figure 2(b); (S-3) an adaptable cuboidal porous composite specimen identical to the cuboidal porous sample S-2, but with 2.5 mm steel balls inside the major pores, see Figure 2(c). All of them were 3D-printed from a high quality ABS material produced by *Rigid.Ink* using a commercial 3D-printer *FlashForge Creator PRO* with the nozzle of diameter 0.4 mm, and a heated bed. High resolution settings were adopted while generating the associated G-code in a slicing software, namely, the layer height of 0.08 mm, 0.4 mm extrusion width, and a 100% infill. The fabrication time ranged from over 11 hours for the cylindrical sample to about 18 hours for the cuboidal samples.

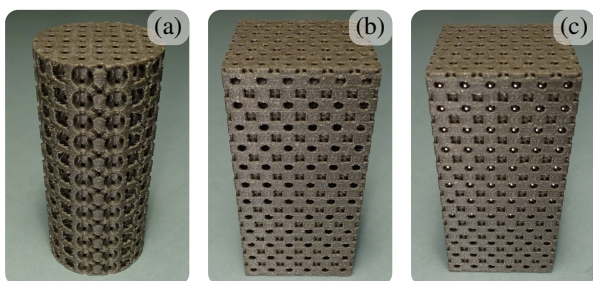


Figure 2: 3D-printed samples: (a) non-adaptable cylindrical sample; (b) non-adaptable cuboidal sample; (c) adaptable cuboidal composite specimen with valve balls (some of them are visible through windows on the lateral side of the sample).

The porous specimens are based on the same three-dimensional array of periodic cells, namely, $6 \times 6 \times 12$ cells, each 5 mm in

size, and hence, each sample height is $12 \times 5 \text{ mm} = 60 \text{ mm}$. The length of the square base edge of both cuboidal samples is $6 \times 5 \text{ mm} = 30 \text{ mm}$, while the diameter of the cylindrical sample is 29 mm. The cylindrical sample perfectly fits inside the metal impedance tube, while for the cuboidal samples a square tube extension with the internal size of 30 mm is required. Such a special impedance tube extension composed of a square tube and a circle-to-square cross-section adapter equipped with a mounting thread was designed and 3D-printed together with a movable plunger that fits well inside the square tube which can be firmly attached to a circular metal impedance tube (see Figure 3). For all acoustical measurements presented in this work, the commercial Bruel&Kjaer impedance tube kit with two high quality microphones was used; the maximum operational frequency range for tube diameter 29 mm is from 500 Hz up to 6300 Hz.

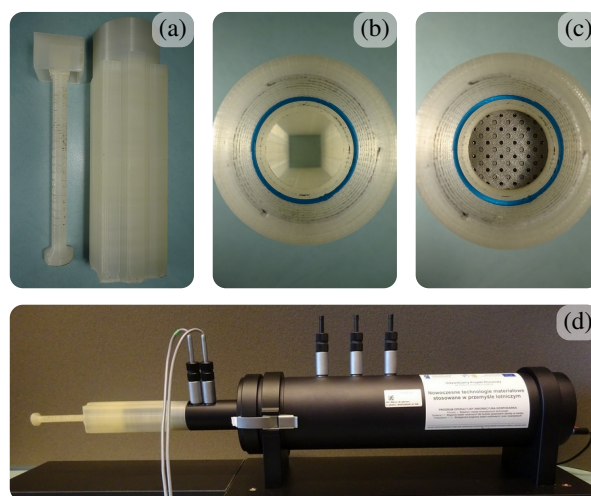


Figure 3: Impedance tube extension (the square tube with the circle-to-square adapter): (a) general view of the 3D-printed square tube extension with the plunger (outside); (b) top view of the adapter with the empty square tube (no sample nor plunger inside); (c) the same top view but with one of the cuboidal samples inside the square tube (only a circular part of the sample top face is visible); (d) 3D-printed square tube extension/adapter fixed to the circular metal impedance tube set-up.

The adaptable cuboidal sample contains small steel balls which were inserted into its largest pores during the fabrication process, see Figure 4. In order to facilitate and speed-up the insertion procedure, an additional tool was designed and fabricated to allow for precise insertion of all balls at once to the manufactured pores. It consists of two components: a thin paddle and a perforated plate with $6 \times 6 = 36$ holes of the size slightly larger than the diameter of the steel balls, see Figure 4(a). Photographs in Figure 4 give a broad idea about the whole operation. At the beginning of extrusion activities, the printer is programmed to pause at certain heights subtly above the localisations of pore centres (i.e., there are twelve stops in total corresponding to twelve layers of cells in the sample). When the machine is forced to have a halt and goes into standby mode, the tray with 36 balls in its holes is accurately placed on the constructed part due to the presence of guideways on its sides, see Figure 4(c,e). Then, one withdraws the paddle from the perforated plate so that the balls fall into the right places and the additive manufacturing process is promptly re-started; the tops of all balls are slightly below the current printing level, so that no collision is possible with the printer nozzle.

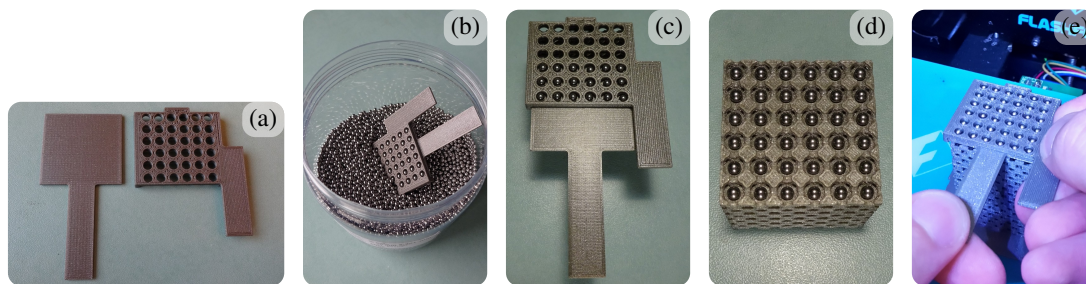


Figure 4: Insertion of steel balls into the major pores of the adaptable sample: (a) the dismantled insertion tray; (b) scooping 36 balls with the tray; (c) pouring 36 balls into the major pores using the insertion tray sat on a sample; (d) 36 balls inside the main pores of an unfinished sample at a certain level; (e) quick pouring of 36 balls into the major pores of sample during the 3D-printing process.

3.3 Sample quality and manufacturing setbacks

The printed samples are of acceptable quality in general. Essentially there are no strings of plastic inside the pores, the inner and outer walls are more or less smooth, and the dimensions are kept (with the repetitive deviation of about -0.12 mm shown at the microscope photograph in Figure 5). However, during and just after the manufacturing process of the structures with steel balls several defects were encountered, unfortunately. First of all, it turned out that the problem of rapid build room cooling on stops was exceptionally difficult to overcome. Even very short breaks necessary to feed balls into pores usually ended with a drop of temperature sufficient to weaken the bonds connecting successive layers such that slight slits typically occurred on the solid surface. The undesired phenomenon was especially visible on the corner edges where the adhesion between two neighbouring layers was the puniest. Sometimes, when the waiting time of the machine was elongated and the bed cooled down below, say, 40°C , the gluing ability of the plastic was reduced to such a level that the filament exiting the extruder did not stick to the existing material, ruining the whole, initially good print, or the final part was about to separate.

The second issue is the quality of the internal surfaces of the 3D-printed impedance tube square extension and the match-up of the plunger. As a matter of fact, two basic mechanisms for the spurious increase of absorption can be distinguished in the case of these 3D-printed auxiliary objects, namely: square tube surface roughness and overall leakiness. Smooth and uniform inner walls have to be kept in order to prevent any sound leakages and ensure similarity with the modelled ideal geometry. On the other hand, the guarantee of an airtight sealing around the medium (of course, except the top surface) is equally crucial, particularly where the sliding plunger come into contact with the walls of the square impedance tube. Nevertheless, the manufactured part of the tube, due to technical reasons, does not fulfil these requirements ideally, although, its quality is generally satisfactory, so that the dissipation of acoustic wave energy for a 60 mm air gap is comparable for both types of impedance tube (see Figure 6): it is obviously a little bit larger for the 3D-printed tube (especially around 3 kHz), but still sufficiently small to be neglected. Moreover, the porous specimen fits well inside the square tube and the plunger moves with the palpable resistance. We suppose, however, that better finish of the inner faces and tweaked obstruction of the tube behind the sample would contribute to the improvement in agreement between numerical and experimental results compared in Section 5.

4 Microstructure-based modelling

4.1 Equivalent fluid approach

The non-adaptable (i.e., without balls) and adaptable (i.e., with valve balls) porous samples are rigid and have an open porosity filled with air. Thus, the investigated porous media can be conceptually substituted by an effective fluid that accurately reflects their macroscopic acoustic characteristics [27].

The effective properties of equivalent fluid, i.e., the effective density ρ_{eff} and bulk modulus K_{eff} are complex-valued and frequency-dependent functions, directly related to some (constant and real-valued) properties of the air saturating the pores (in particular, its density ρ_0 and bulk modulus K_0), namely,

$$\rho_{\text{eff}}(\omega) = \frac{\rho_0 \alpha(\omega)}{\phi}, \quad K_{\text{eff}}(\omega) = \frac{K_0}{\phi \beta(\omega)} \quad (1)$$

with $\beta(\omega) = \gamma - \frac{\gamma - 1}{\alpha'(\omega)}$.

Here, $\omega = 2\pi f$ is the wave angular frequency (f is the frequency), ϕ is the porosity, and γ is the heat capacity ratio (the adiabatic index) for air, while $\alpha(\omega)$ and $\alpha'(\omega)$ are the dynamic visco-inertial and dynamic thermal tortuosity functions, respectively.

There exist semi-phenomenological models [27] that describe the two dynamic tortuosity functions, $\alpha(\omega)$ and $\alpha'(\omega)$, in terms of several real-valued transport parameters of a porous material (additional parameters are the kinematic viscosity and Prandtl number for air – the fluid which saturates the pores) – see Appendix A). The transport parameters are related purely to the micro-geometry of solid skeleton and they can be computed from microstructure provided that a periodic volumetric cell representative for that microstructure is available.

4.2 Micro-geometry survey and geometrical model adjustments

In the case of standard porous media fabricated using various physico-chemical processes, which usually involve a lot of chaotic deviations, representative periodic cells can be constructed (based on some microscope survey or computer tomography scans) as some kind of approximations for not exactly periodic microstructure. On the other hand, the porous media fabricated using the additive manufacturing technologies (like the ones in this research) are usually based on a designed periodic cell which is repeated to form a periodic array of a bulk of porous material. Therefore, the

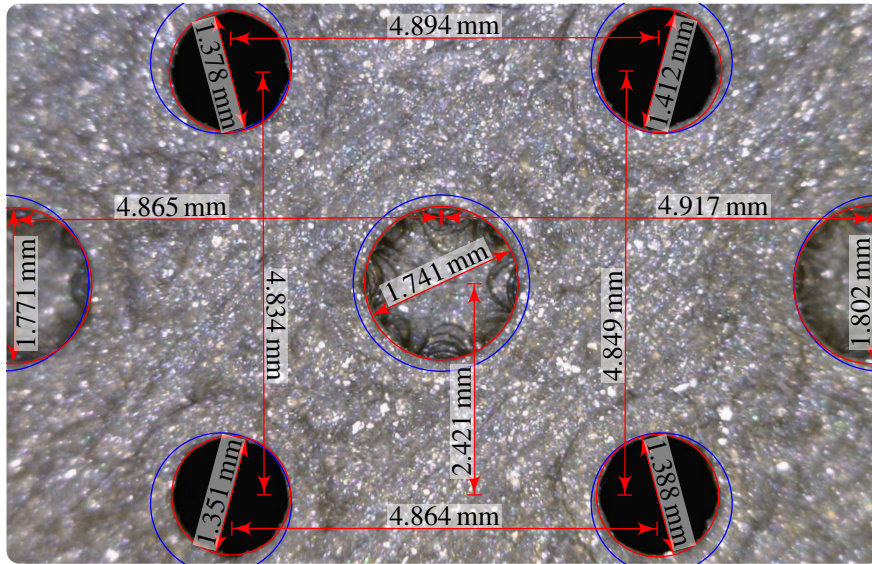


Figure 5: Microscopic measurements of actual dimensions (in red) for one of the fabricated samples (top view) indicating deviations from the designed dimensions and shapes (in blue).

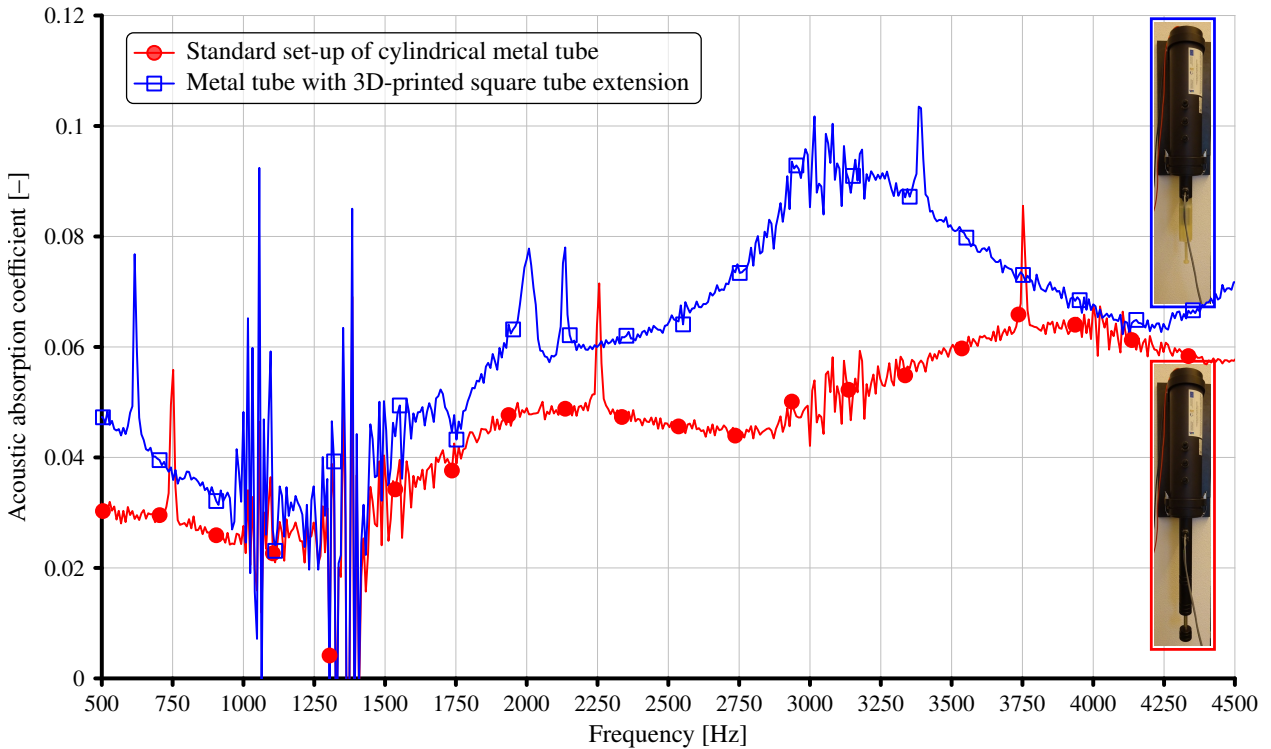


Figure 6: Negligible sound absorption and leakage measured for 60 mm air cavities in the *empty* impedance tubes: the standard cylindrical tube made of metal, and the modified set-up with the attached square tube extension (fabricated from ABS) replacing a part of the circular metal tube.

periodic representative micro-geometry is known *a priori*, however, one *must* verify it through a microscope survey, and then, usually, it must be updated in order to serve for the calculations based on truly actual microstructure.

A simple microscope survey carried out for the 3D-printed samples (see Figure 5) allowed to update the designed periodic volumetric cell in order to more correctly represent the actual fabricated micro-geometry. Thus, taking into account the incompatibility between the actual dimensions of the manufactured samples and the designed values (see Figure 5), all the radii of pores and channels in the pore network shown in Figure 1(a) were decreased by 0.12 mm

and this updated geometry of the fluid Representative Volume Element (see Figure 1(f)) was used in all final calculations. In particular, it entailed the drop of porosity from about 52% to 43% for the case without ball, and from 46% to 37% when the 2.5 mm ball is set inside the main pore of the cell. The new values of the diameters are listed in Table 2.

In the adaptive configuration the steel ball centre is set 1 mm below the centre of the large pore, which means that a narrow aperture (approximately 0.019 mm) is left between the ball surface and the edge of the wide channel below. This thin regular slit is left to simulate a leaky contact between the smooth steel ball and the rough

Table 2: Diameters of pores and channels in the actual periodic cell of size 5 mm – as determined from the fabricated samples to update the fluid domain used for calculations.

Void type	Diameter [mm]
large pore	4.36
small pore	1.76
wide channel	1.36
narrow channel	0.76

3D-printed edge of the channel, which in principle is not uniform and varies from cell to cell. Due to the existing irregularities arisen at the production stage, the channel can only be partially blocked by the steel ball but not fully sealed.

4.3 Calculations of transport parameters

In this work, the dynamic tortuosity functions $\alpha(\omega)$ and $\alpha'(\omega)$ (and hence, the effective properties of equivalent fluid) are estimated using the Johnson-Champoux-Allard-Pride-Lafarge (JCAPL) model [21, 23–27] for rigid-frame sound-absorbing porous media (see Appendix A for the JCAPL model formulas). This model is essentially based on *eight* transport parameters, namely, the porosity, viscous permeability, thermal permeability, (inertial) tortuosity, static viscous tortuosity, static thermal tortuosity, and two characteristic lengths: viscous and thermal one; all of them can be evaluated from a porous microstructure [33, 34, 46–48, 50]. The overall porosity and thermal characteristic length are computed directly from the micro-geometry, without solving any additional equation. The remaining six parameters are based on the volume-averaged solutions of three steady-state Boundary Value Problems (BVPs) defined at the micro-scale level on the periodic fluid domain, namely: the static viscous permeability and tortuosity parameters are obtained from the Stokes flow problem; the static thermal permeability and tortuosity are calculated from the solution of the Poisson equation; finally, the inertial tortuosity and the viscous characteristic length are evaluated after solving the Laplace equation. The first BVP describes a steady, incompressible, viscous flow through a porous network (i.e., pores and channels) of the periodic representative cell with no-slip boundary conditions on the solid walls. The Poisson equation describes the thermal dispersion inside the fluid domain with thermostatic boundary conditions on the solid surfaces, whereas the Laplace problem simulates the electric conduction in a porous medium with a dielectric skeleton saturated by an electrically conductive pore-fluid, since at very high frequencies the viscous effects are negligible and the incompressible flow of *inviscid* fluid coincides formally with such an electrical problem. Therefore, a typical experiment to determine the (inertial) tortuosity of a porous medium with known open porosity is as follows: the pore network is filled with a fluid of a known electric conductivity and an electric current is applied to measure the effective electric conductivity of such a saturated porous composite; since the conductivity of the saturating fluid and the porosity are known *a priori* the tortuosity can be computed from the measured effective conductivity. Note, however, that such a (non-acoustical) experiment can be carried out only when the solid matrix is wholly made up from a dielectric material, so it is not possible in the case of the porous composite, because of the

presence of steel valve balls. On the other hand, numerical calculations can always be carried out simply by assuming that the balls are *not* made of metal. Finally, to capture the periodic architecture of the proposed medium, in each analysis the appropriate periodic boundary conditions are set on the fluid boundaries lying on the side faces of the cubic RVE.

In the case of the Stokes problem, the flow is driven by an external pressure gradient which forms a uniform vector field over the whole fluid domain in the periodic cell. The cause is, therefore, directional and the chosen direction corresponds to the macroscopic direction of acoustic wave propagation. Note also that the calculation of the (static) permeability by solving the linear Stokes' equation (where the inertial effects are not present) is fully correct, because the real airflow inside all pores is due to very small oscillatory fluctuations caused by acoustic waves which penetrate the porous absorber saturated with air. In the case of the Laplace problem, the cause has also a vectorial character: it is a constant external electric field applied in the propagation direction (uniformly over the whole fluid domain). Consistently, the solutions of these two problems (or their averages over the fluid domain) are projected on the propagation direction. This directional dependency is used in the case of the proposed adaptable absorber, where the valve ball may be shifted inside the pore so that it blocks or disturbs the path of viscous flow or electric field in different way, which entails a change in the corresponding transport parameters. In the case of the Poisson problem, the cause for thermal dispersion is non-directional: it is a scalar field of heat source uniform over the whole fluid domain. Since the three problems are linear, the uniform vector fields (the pressure gradient and the electric field) as well as the scalar field (of heat source) are (usually) normalised to the dimensionless unity (i.e., the unit vector or unit scalar field, respectively) and in that way the linear problems are appropriately re-scaled.

Two periodic volume meshes shown in Figure 7 were generated for the updated (i.e., actual) micro-geometry of the fluid domain in the periodic cell with and without the valve ball. They served in finite element calculations of transport parameters for the following three cases:

1. the non-adaptable cell, i.e., *without* ball (Figure 7(a));
2. the adaptable cell with ball at the bottom (Figure 7(b)) – for the *horizontal* direction of wave propagation;
3. the adaptable cell with ball at the bottom (Figure 7(b)) – for the *vertical* direction of wave propagation;

In the case of the non-adaptable cell (Figure 7(a)), there is no distinction between the vertical and horizontal directions of wave propagation (because of the full symmetry of the cell without ball). On the other hand, when modelling the adaptable cell (Figure 7(b)), the valve ball is always at the bottom of the major pore and only the propagation direction is set either as vertical or horizontal with respect to this configuration in order to consider each of the two extreme cases. One should notice that from the macroscopic perspective it is the ball which is shifted whereas the wave propagation direction remains the same, that is, at normal incidence to the surface of the (panel or sample of) adaptive absorber composed from such small periodic cells. Further, it will be shown that by shifting the ball (with the gravity force) the sound absorbing panel is

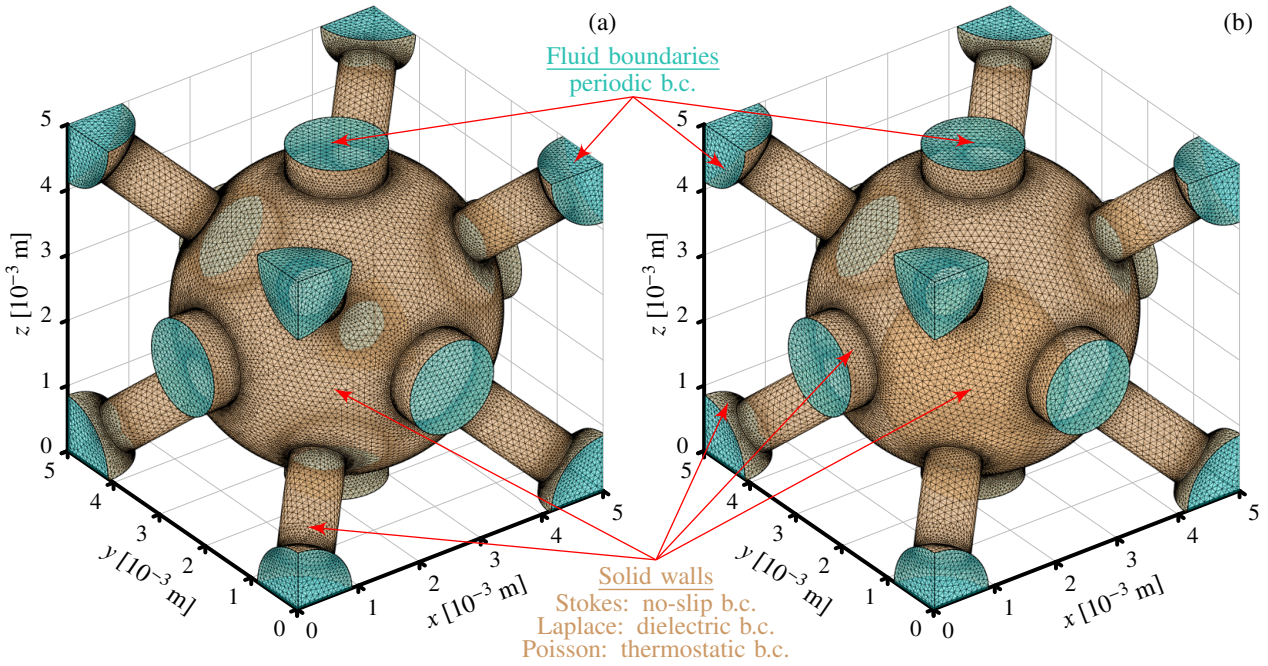


Figure 7: Finite element meshes of the representative volume element: (a) the non-adaptable cell without ball (570686 finite elements), and (b) the adaptable cell with ball (576339 finite elements).

adapted to different noise conditions. In Figure 7 the fluid boundaries with periodic boundary conditions are distinguished, as well as the solid walls of the skeleton and valve ball under appropriate conditions, namely: the no-slip (i.e., zero velocity) boundary conditions for the Stokes flow, the thermostatic (i.e., zero temperature) boundary conditions for the Poisson's problem, and the dielectric boundary conditions for the Laplace's problem, i.e., the electric field component normal to a solid boundary is set to zero (even for the valve ball, because in the calculations all solid material is treated as a dielectric).

The transport parameters for all three cases were calculated and their values are listed together in Table 3. For the cell without ball these parameters remain the same for the vertical and horizontal propagation directions (defined along the wide channels), and the transport is mainly directed through those pairs of the wide channels which are parallel to the propagation direction. On the other hand, when the valve ball is present inside the cell, the wide channels parallel to the propagation direction can be still left open (the horizontal direction case) or they can be almost fully blocked by the ball (the vertical direction case). This latter case leads to a significant increase of the inertial and viscous tortuosities, and to even more significant decrease of the viscous permeability and characteristic length. This phenomenon is well illustrated in Figure 8 which compares the character of viscous flows through the periodic RVE in each case (by showing the velocity fields scaled to the unit of permeability): when the external pressure gradient direction is parallel to the axis of the channel blocked by the ball, i.e., for the 'vertical' wave propagation in the adaptable material (see Figure 8(c)), most of the flow goes through the oblique, narrow channels; otherwise, the main flow passes predominantly through the wide channels, i.e., for the 'horizontal' wave propagation in the adaptable material (see Figure 8(b)), or for the non-adaptable material where there are no valve balls in the cells (see Figure 8(a)). Similarly, significant differences are visible between the results of

the 'vertical' and 'horizontal' cases of Laplace analyses (see Figure 9 where the scaled fields of electric potential are compared) which allow to determine the inertial tortuosity and viscous length, while for the thermal parameters only a single Poisson analysis is computed for the periodic cell with the valve ball, just like for the cell without ball (see Figure 10 where the corresponding thermal fields scaled to the unit of permeability are shown).

The porosity and thermal transport parameters shown in the two last columns of Table 3 for the adaptable cell are obviously always the same, no matter is the propagation direction; they differ – although not very much – from the corresponding values of the non-adaptable cell. Also for the horizontal direction case of the adaptable cell, that is, when the axis of the channel blocked by the valve ball is perpendicular to the main transport direction, the inertial tortuosity and all viscous parameters tend to be *not* very much different from the corresponding quantities obtained for the non-adaptable cell without ball (with deviations ranging from almost 6% to 13%). However, for the vertical propagation direction, the viscous and inertial tortuosities are significantly larger, while the viscous permeability and characteristic length are much smaller than their counterparts computed for any of the two other cases. Thus, these four (out of eight) transport parameters depend on the direction of wave propagation and can significantly change their values due to the relative position of the valve ball, which will eventually cause different sound absorption in such an adaptable or adjustable material.

5 Macroscopic analyses and experimental verification

The distribution of acoustic pressure in the equivalent fluid (and in the adjacent layer of air) was found after performing three-dimensional macroscopic numerical analyses on (the quarters of)

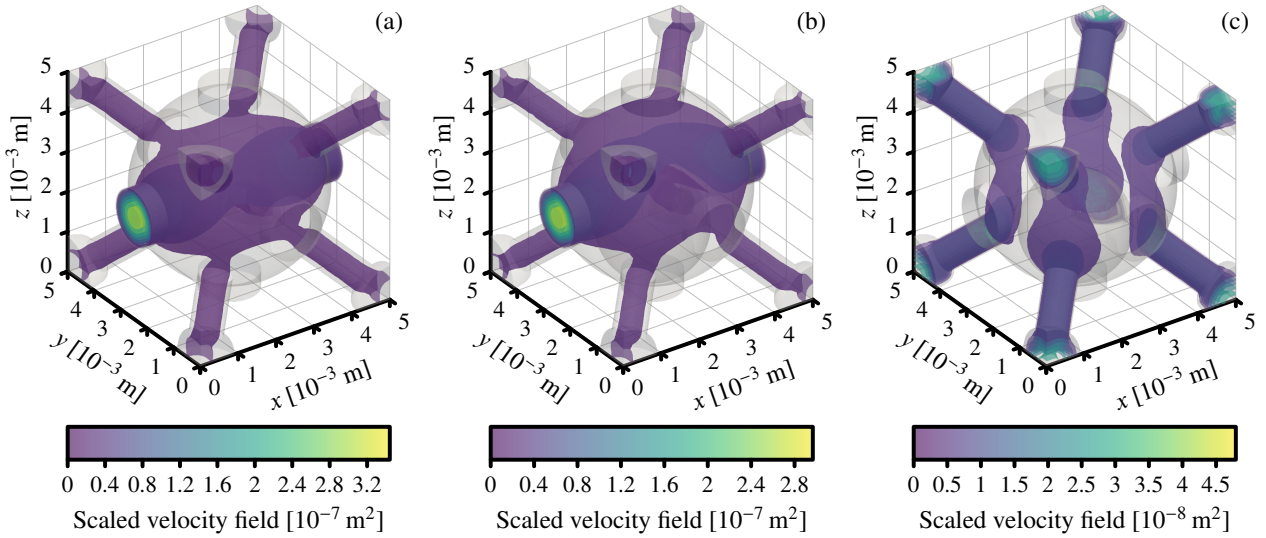


Figure 8: Viscous flow through the periodic representative cell: (a) with empty pores, and (b,c) with a sphere (valve ball) at the bottom of the main pore; the pressure gradient driving the flow is in the horizontal x -direction (a,b), or in the vertical z -direction (c), which in each case is related to the macroscopic direction of wave propagation.

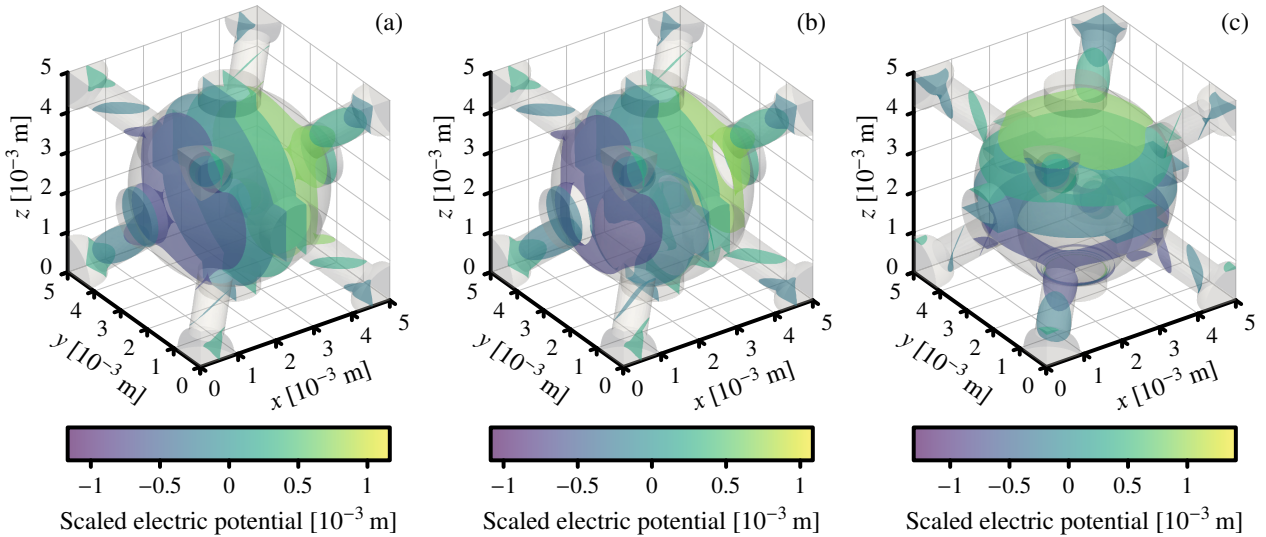


Figure 9: Electric conduction within the representative cell: (a) with empty pores, and (b,c) with a sphere (valve ball) inside the main pore, at the bottom of it; the external electric field, which causes the electric potential field, is in the horizontal x -direction (a,b), or in the vertical z -direction (c).

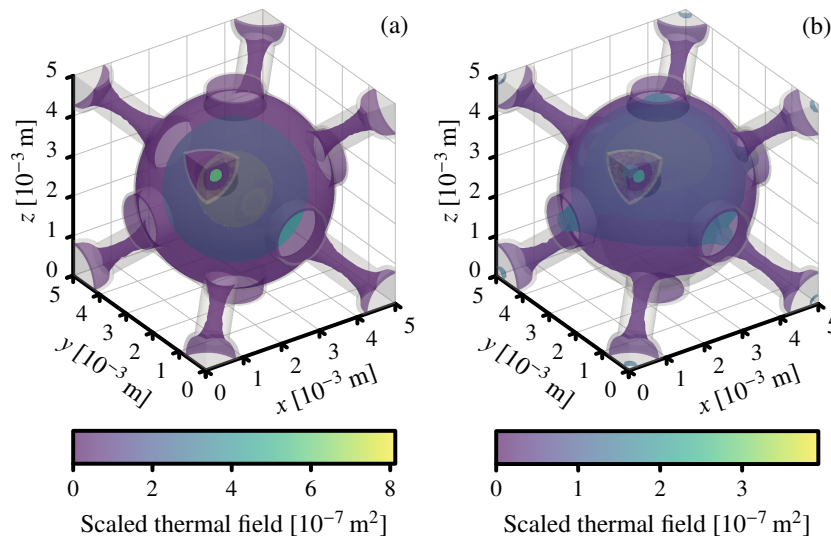


Figure 10: Thermal dispersion within the representative cell: (a) with empty pores, and (b) with a sphere (the valve ball) inside, that is, at the bottom of the main pore.

Table 3: Transport parameters calculated for the periodic representative cells.

Transport parameter	Symbol	Unit	Non-adaptable cell (without ball)	Adaptable cell – horizontal case	Adaptable cell – vertical case
(open) porosity	ϕ	%	43.43	36.89	36.89
viscous permeability	k_0	10^{-9} m^2	11.93	10.37	1.737
thermal permeability	k'_0	10^{-9} m^2	121.9	45.32	45.32
(inertial) tortuosity	α_∞	–	2.040	1.900	2.767
static viscous tortuosity	α_0	–	3.384	3.189	5.881
static thermal tortuosity	α'_0	–	1.611	1.666	1.666
viscous characteristic length	Λ	mm	0.606	0.551	0.145
thermal characteristic length	Λ'	mm	1.199	0.837	0.837

the cylindrical and cuboidal domains. They were conducted for the porous media discussed in the previous sections, that is, for the material without balls and for the adaptable composite with valve balls in two different positions with respect to the direction of wave propagation. From the perspective of the transport parameters that characterize porous media, one may speak here, in fact, about three distinct materials. Consequently, three analyses were carried out for each of the three sets of parameters from Table 3 (i.e., nine macroscopic analyses of sound propagation in total), namely:

1. a one-dimensional analytical study of plane waves propagating in air and penetrating into a porous medium at normal incidence to its surface (see, for example, [63] for complete analytical formulas for single- and double-layer configurations).
2. a three-dimensional finite element simulation on a quarter of porous cylinder with an adjacent layer of air (see Figure 11(a) for the corresponding mesh).
3. a three-dimensional finite element analysis on a quarter of porous cuboid with an adjacent quarter of cylinder of air (the corresponding mesh is shown in Figure 11(c)).

As depicted in Figure 11, an adjacent layer of air was added above the porous regions to guarantee that the acoustic waves are *planar* at the top surface (i.e., at some distance above the porous cuboid), where the surface acoustic impedance is to be evaluated in order to determine sound absorption. Notice that because of the symmetry of the analysed three-dimensional macroscopic problems, only the relevant quarters of the porous and air domains were considered (see Figure 11). The height of the air layer is 20 mm, and it is one-third of the height of porous domains (this height of 60 mm comes from twelve layers of periodic RVEs). The diameter of cylindrical domains is 29 mm and the full width of the cuboid is 30 mm (which means 15 mm for the base edge of a quarter of the cuboid).

The Helmholtz equation of linear acoustics was solved to predict the propagation of waves in the discretised regions of porous composites and air. The equivalent fluid characteristics (1) available for the porous composites thanks to the determined transport parameters and the JCAPL model (see Appendix A) were utilized to compute the effective speeds of sound in the investigated porous media:

$$c_{\text{eff}}(\omega) = \sqrt{\frac{K_{\text{eff}}(\omega)}{\rho_{\text{eff}}(\omega)}} = \frac{c_0}{\sqrt{\alpha(\omega)\beta(\omega)}}. \quad (2)$$

The real part of c_{eff} is always (i.e., at each frequency for any porous medium) smaller than $c_0 = \sqrt{K_0/\rho_0}$, that is, the speed of sound in air (which saturates the pores).

In both macroscopic configurations (see Figure 11) the sound-hard boundary condition was applied on the lateral surfaces representing symmetry planes, as well as on the other lateral and bottom sides serving as rigid walls (i.e., to simulate the metal walls of the cylindrical impedance tube and the plastic 3D-printed walls of the cuboidal tube extension, which together with their closing plungers play the role of rigid terminations in the case of the cylindrical and cuboidal specimens, respectively). The rigid-wall condition was also set on the ‘external’ part of the top surface of the cuboidal porous domain (the ‘internal’ part of this top surface forms the interface with the neighbouring cylindrical air layer).

On the top surface of the air layer added above the porous region in both macroscopic configurations shown in Figure 11, the pressure boundary condition is applied to simulate the plane acoustic wave propagating into these domains. In the case of the purely cylindrical system, i.e., the one with the (quarter of) porous cylinder as in Figure 11(a), the wavefronts are planar everywhere and the problem and all results are in fact unidimensional, that is, they are constant on all quarter-circle cross-sections (see Figure 11(b)) and their variations along the cylinder height should be the same as the corresponding results obtained analytically. In fact, the main purpose of this numerical analysis was to check the applied finite element modelling. The one-dimensional problem and the corresponding three-dimensional cylindrical configuration simulate the plane wave propagation in the impedance tube with the cylindrical porous sample (or, in a vast porous layer of the same thickness as the sample height), and their solutions are practically the same as confirmed by the results presented further in Figures 12–14.

In the configuration with the porous cuboid, see Figure 11(c), the wave propagation is a little bit more complex and to some point three-dimensional (that is, in the region close to the interface between the air and porous medium), although the waves are still planar in the air domain slightly away from the porous cuboid and they become planar again inside the porous cuboid away from its top surface, see Figure 11(d). This configuration serves to model the case where the plane acoustic waves propagate in the cylindrical metal impedance tube and pass into the 3D-printed cuboidal absorber located within the plastic tube which terminates the measurement setup.

When any of the harmonic wave propagation problems is solved, the frequency-dependent complex-valued surface acoustic impedance $Z_s(\omega)$ is computed on the top surface of the air domain, where the wave fronts are planar—as they are, in reality, in the impedance tube (a little bit away from the surface of the porous cuboid absorber) and in particular at the specified locations of two microphones measuring the acoustic pressure, in accordance with

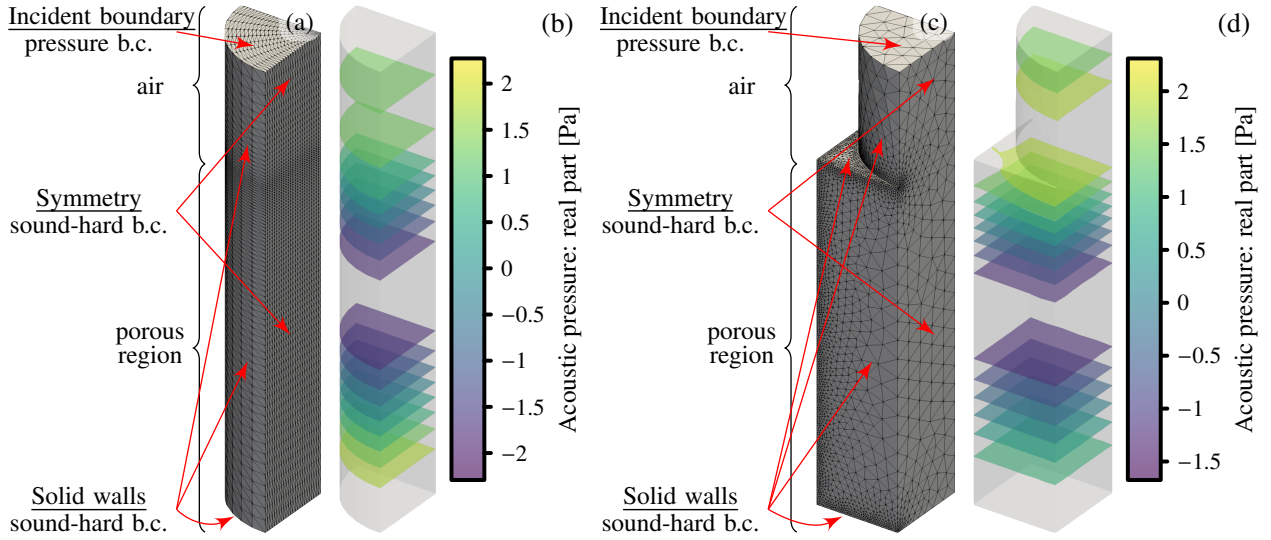


Figure 11: Macroscopic analyses performed of a 60 mm porous domain and an adjacent 20 mm domain (layer) of air: (a) finite element mesh (41050 tetrahedra) on the quarter of the adjacent cylindrical porous and air domains; (b) acoustic pressure distribution at 3.2 kHz inside (the quarter of) the cylindrical porous and air domains; (c) finite element mesh (53309 tetrahedra) on the quarter of the cuboidal porous domain and the adjacent cylindrical air domain; (d) acoustic pressure distribution at 3.2 kHz inside (the quarter of) the cuboidal porous domain and the adjacent cylindrical air domain.

the Two-Microphone Transfer Function Method [64]. The (computed or measured) surface acoustic impedance $Z_s(\omega)$ together with the known characteristic impedance of air $Z_0 = \rho_0 c_0$ allow to determine the real-valued acoustic absorption coefficient $\mathcal{A}(\omega)$ in the considered frequency range [27, 64]:

$$\mathcal{A}(\omega) = 1 - |\mathcal{R}(\omega)|^2, \quad \mathcal{R}(\omega) = \frac{Z_s(\omega) - Z_0}{Z_s(\omega) + Z_0}. \quad (3)$$

The wave propagation in the air domain (outside of the porous materials) is lossless, so the sound absorption computed for the meshed configurations depicted in Figure 11 comes only from the porous absorbers.

Figure 12 presents the sound absorption results for the non-adaptable porous material, i.e., without balls, so in that case, the cylindrical sample could be manufactured, and the predictions can be compared with the corresponding measurements obtained not only for the porous cuboid, but also for the porous cylinder. The analytical result and numerical calculations for the cylinder are similar with the experimental curve for the cylindrical sample when the peaks in absorption are compared, however, there is some underestimation at frequencies between the peaks (where the acoustic absorption is low, anyway). The same is observed when comparing the numerical predictions for porous cuboid with the corresponding experimental curve, although in that case the discrepancies are slightly larger. Figure 12 shows also the absorption curve computed analytically for the initial, that is, *not* updated micro-geometry. The peaks of this curve are shifted in frequency with respect to the relevant experimental curve pertaining to the 3D-printed cylindrical sample, which confirms the necessity of adjustment of some crucial pore network dimensions to the actual values measured under the microscope.

The results obtained for the adaptable material with valve balls are shown in Figures 13 and 14 for the two extreme cases, that is, when:

1. the valve balls block the channels *perpendicular* to the direction of wave propagation, which means that the impedance

tube with the adaptable porous sample is set in the *horizontal* position (i.e., put on the table)—see Figure 13;

2. the valve balls block the channels *parallel* to the direction of wave propagation, which means that the impedance tube with the adaptable porous sample is set in the *vertical* position (i.e., hung on the wall)—see Figure 14.

Figure 13 presents the acoustic absorption of waves propagating in the horizontal direction in the layer and sample of the adaptable material—with respect to the vertical gravity force. Generally speaking, the character of absorption curves in that case is quite similar to the absorption presented in Figure 12 for the material without valve balls, although the porosity and other transport parameters are rather different. The analytical results (valid for the layer of such absorbing material) are the same as the corresponding numerical calculations for the cylinder. As expected, the numerical predictions for the adaptable porous cuboid absorber are closer to the measurements (possible only for the cuboid sample) than other calculations: in particular, a small relative shift of absorption peaks to slightly lower frequencies is very well predicted.

The predictions shown in Figure 14 for the adaptable porous cuboid in vertical position are quite accurate below 2.5 kHz, and only with some moderate discrepancies at higher frequencies. In general, the low-frequency absorption peaks and the overall character of sound absorption are very well assessed. In fact, a similar shape of the absorption curve is also predicted by the analytical and numerical calculations made for the porous cylinder.

By comparing the results shown in Figures 13 and 14, one can see that the absorption of sound waves propagating in the vertical direction in the adaptable porous material, (i.e., in the direction of the gravity force, see Figure 14), is completely different than in the case of the horizontal propagation (i.e., across the direction of gravity force, see Figure 13). In order to better see that difference, the numerical and experimental results obtained for the cuboid adaptable sample are re-plotted together in Figure 15. It is clear that the overall absorption tends to be generally better for the vertical position, however, there are wideband frequency ranges where

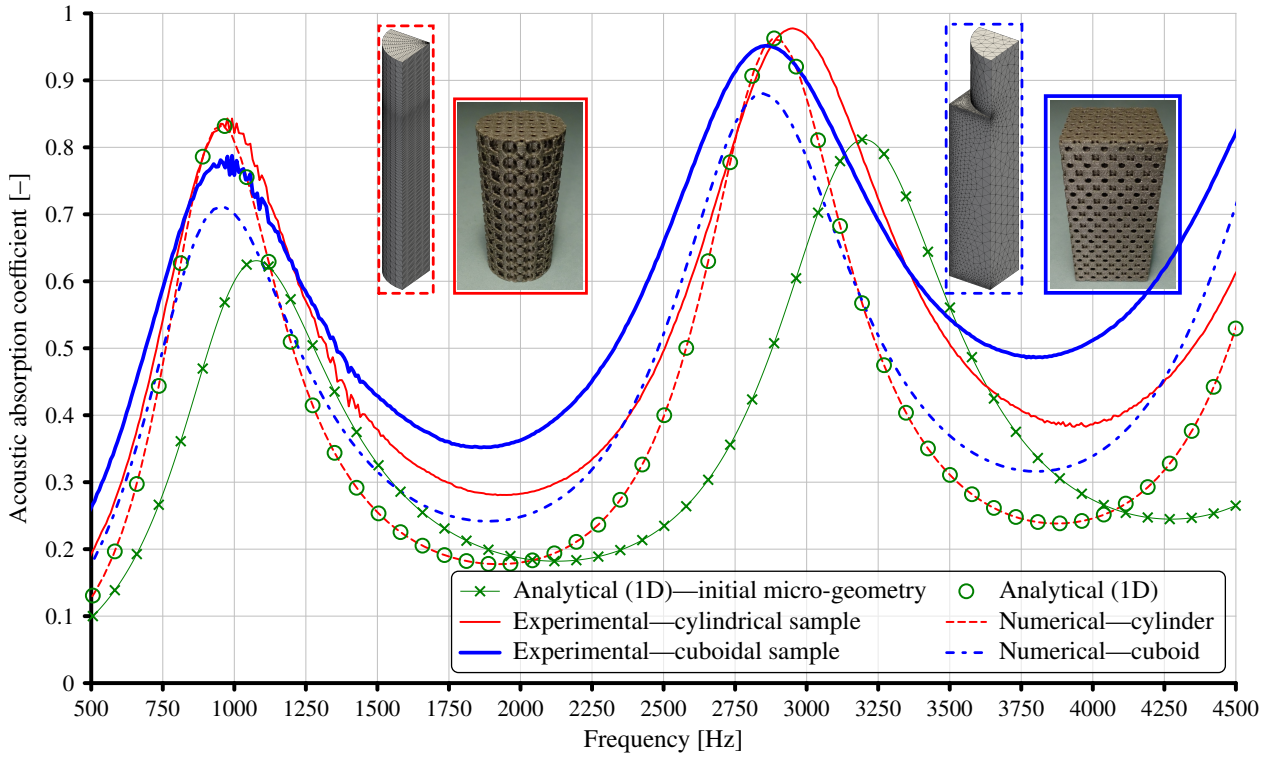


Figure 12: Sound absorption coefficient for the non-adaptable material (i.e., without balls).

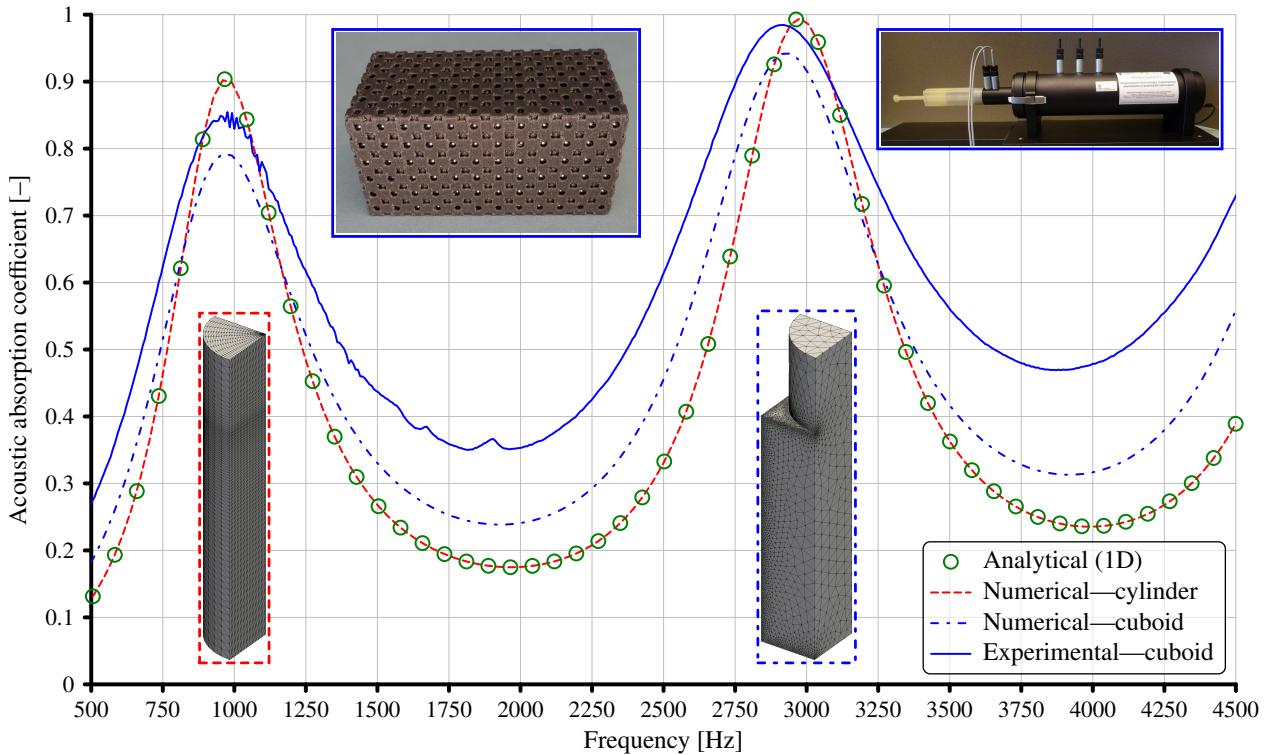


Figure 13: Sound absorption coefficient for the layer and sample of the adaptable composite material (i.e., with valve balls) and the horizontal propagation direction (the tube with the adaptable sample set horizontally on the table).

the horizontal position ensures the best absorption: for example, around 2.9 kHz a local minimum in absorption of the adaptable porous material in the vertical position can be changed to a local maximum (in fact, a nearly perfect absorption) of the horizontal position. More precise and quantitative observations can be stated

as follows. After changing the absorber from the horizontal to vertical position, the three absorption peaks are dramatically shifted in the frequency from about 1 kHz and 2.9 kHz to lower values of about 0.7 kHz and 2.1 kHz, respectively. In the vertical position, the mentioned lowest-frequency absorption peak reaches 1.0,

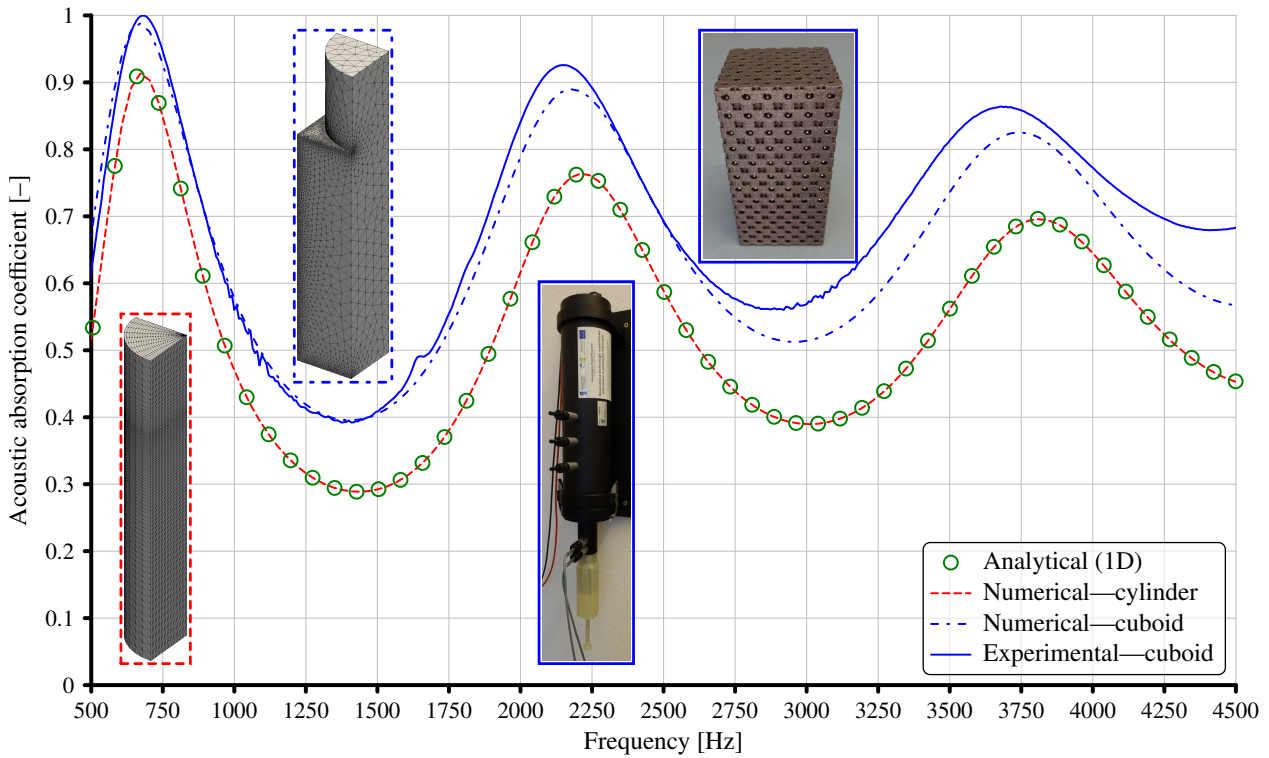


Figure 14: Sound absorption coefficient for the layer and sample of the adaptable composite material (i.e., with valve balls) and the vertical propagation direction (the tube with the adaptable sample hanging vertically on the wall).

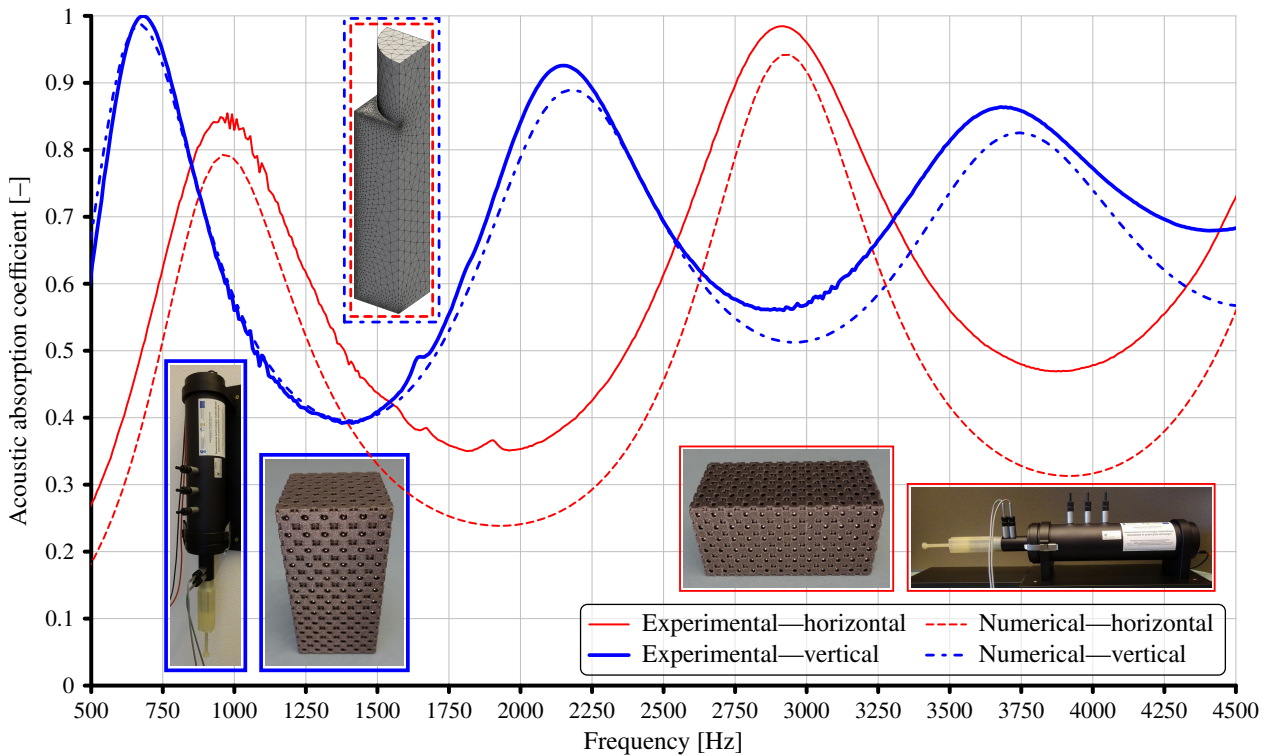


Figure 15: Comparison of the experimental and numerical results for the adaptable composite absorber (i.e., the porous cuboid with valve balls)—for the horizontal and vertical propagation directions.

the next peak is about 0.92, and another higher frequency peak (at 3.6 kHz) exceeds 0.86, while in the horizontal position the lowest-frequency peak is about 0.85 and the maximal absorption value of roughly 0.99 is gained by the second peak in the considered frequency range.

6 Conclusions

The sound absorption mechanisms in the proposed porous composite should be interpreted and explained as follows. The presence (or absence) of valve balls has its effect on all transport pa-

rameters, however, the change of their relative position in the periodic cells with respect to the macroscopic direction of the acoustic wave propagation significantly affects only 4 transport parameters (viz., k_0 , α_0 , α_∞ , and Λ) and in that way also the effective speed of acoustic waves. Due to the porous material dispersion this effective speed of sound strongly depends on the frequency; the microstructural modification of local visco-inertial transport (using valve balls) changes this relationship in different ways at different frequencies, which has a very significant impact on wavelength at the macro-scale level. The porous composite absorber was designed to observe the clear quarter wavelength resonance behaviour typical for granular materials [48, 49] and some other porous media (excluding highly porous materials with small pores, e.g., typical PU foams and high-porosity ceramic foams [65]). This behaviour is clearly shown in Figures 12-15 where the acoustic absorption peaks correspond to quarter and three-quarter wavelength layer resonances, and also to a five-quarter wavelength resonance related with the third absorption peak in the case of the composite absorber in vertical position. The frequency of the quarter (three-quarter, five-quarter, etc.) wavelength resonance in the sound absorption spectrum for a hard-backed rigid-frame porous layer can be influenced by the design of its microstructure as well as its thickness [11, 66]. The porous composite thickness is constant, but its microstructure can be modified accordingly by changing the position of valve balls. When the valve balls block the channels parallel to the wave propagation direction, they increase the tortuosities (α_∞ and α_0) which reduces the sound speed and, as a consequence, lowers the frequencies of the quarter wavelength resonances [11, 66] so that a five-quarter wavelength resonance appears in the considered frequency range at app. 3.6 kHz (see Figures 14 and 15); at the same time the viscous permeability k_0 is decreased (as well as the viscous length Λ) which makes the magnitude of peak absorption higher at the quarter wavelength resonance [11, 66] (see Figures 14 and 15). When the porous composite is positioned horizontally, the valve balls do not block the path parallel to the direction of the wave propagation so much, and the sound waves are not so much slowed down, so the overall nature of the sound absorption is similar to that obtained for porous samples without valve balls (cf. Figures 12 and 13).

The proposed concept of an adaptive acoustic composite material proved to be promising and feasible. Obviously, the assumed size of the periodic unit cell (5 mm) was far too large to permit for a more efficient (broadband) sound absorption, however, it was forced by a low precision and poor resolution of the budget 3D-printer of the most common 3D-printing technology (FDM) used for manufacturing. The applied advanced dual-scale modelling was effective, provided correct estimations and made a complex design process possible. The discrepancies between the predictions and measurements are mainly due to imperfections in the manufactured samples like inconsistency in dimensions and shapes, surface roughness, leakages, etc. Furthermore, larger deviations appeared at higher frequencies where acoustic measurements are more sensitive to various specimen flaws. The discrepancies should diminish after using a fabrication technique and device of better quality. The whole process presented in this work (design and modelling, prototyping and manufacturing, experimental validation) proved to be suitable for the development of such adaptive sound-absorbing composites. And with a rapid development of modern additive manufacturing technologies it seems almost certain that in the near

future 3D-printing will be used to produce dedicated acoustic treatments with a designed microstructure.

Acknowledgements

The financial support of Project No. 2015/19/B/ST8/03979: "Relations between the micro-geometry and sound propagation and absorption in porous and poroelastic media", financed by National Science Centre (NCN), Poland, is gratefully acknowledged.

A Formulas of the Johnson-Champoux-Allard-Pride-Lafarge (JCAPL) equivalent-fluid model

The JCAPL model [21, 23–27] requires 8 transport parameters: the porosity ϕ , the (inertial) tortuosity α_∞ , the static viscous and thermal tortuosities α_0 and α'_0 , the static viscous and thermal permeabilities k_0 and k'_0 , and the viscous and thermal characteristic lengths Λ and Λ' .

The dynamic viscous tortuosity function $\alpha(\omega)$ is computed as follows (here, i is the imaginary unit):

$$\alpha(\omega) = \alpha_\infty \left[1 + \frac{\mathcal{F}(\omega)}{i\tilde{\omega}} \right], \quad \mathcal{F}(\omega) = 1 - \mathcal{P} + \sqrt{\mathcal{P}^2 + \frac{\mathcal{M}}{2} i\tilde{\omega}}, \quad (\text{A.1})$$

where the dimensionless frequency $\tilde{\omega}$ for viscous effects (normalised with respect to the kinematic viscosity of air ν , i.e., the fluid which fills the pores), the viscous pore-shape factor \mathcal{M} and low-frequency viscous correction parameter \mathcal{P} are defined as:

$$\tilde{\omega} = \omega \frac{\alpha_\infty k_0}{\phi \nu}, \quad \mathcal{M} = \frac{8\alpha_\infty k_0}{\phi \Lambda^2}, \quad \mathcal{P} = \frac{\mathcal{M}}{4(\alpha_0/\alpha_\infty - 1)}. \quad (\text{A.2})$$

The dynamic thermal tortuosity $\alpha'(\omega)$ is computed as follows:

$$\alpha'(\omega) = 1 + \frac{\mathcal{F}'(\omega)}{i\tilde{\omega}'}, \quad \mathcal{F}'(\omega) = 1 - \mathcal{P}' + \sqrt{\mathcal{P}'^2 + \frac{\mathcal{M}'}{2} i\tilde{\omega}'} \quad (\text{A.3})$$

where the dimensionless frequency $\tilde{\omega}'$ for thermal effects (normalised with respect to $\nu' = \nu/N_{Pr}$ with N_{Pr} being the Prandtl number for air), the thermal pore-shape factor \mathcal{M}' and low-frequency thermal correction parameter \mathcal{P}' are defined as:

$$\tilde{\omega}' = \omega \frac{k'_0}{\phi \nu'}, \quad \mathcal{M}' = \frac{8k'_0}{\phi \Lambda'^2}, \quad \mathcal{P}' = \frac{\mathcal{M}'}{4(\alpha'_0 - 1)}. \quad (\text{A.4})$$

References

- [1] Shi X., Wu J., Wang X., Zhou X., Xie X., Xue Z., Novel sound insulation materials based on epoxy/hollow silica nanotubes composites, *Composites Part B* 2017; 131:125–133.
- [2] Tiuc A. E., Nemeş O., Vermeşan H., Toma A. C., New sound absorbent composite materials based on sawdust and polyurethane foam, *Composites Part B* 2019; 165:120–130.
- [3] Yang Y., Li B., Chen Z., Sui N., Chen Z., Saeed M.-U., Li Y., Fu R., Wu C., Jing Y., Acoustic properties of glass fiber assembly-filled honeycomb sandwich panels, *Composites Part B* 2016; 96:281–286.
- [4] Boutin C., Acoustics of porous media with inner resonators, *J. Acoust. Soc. Am.* 2013; 134:4717–4729.

- [5] Groby J.-P., Lagarrigue C., Brouard B., Dazel O., Tournat V., Nennig B., Using simple shape three-dimensional rigid inclusions to enhance porous layer absorption, *J. Acoust. Soc. Am.* 2014; 136:1139–1148.
- [6] Boutin C., Bécot F.-X., Theory and experiments on poro-acoustics with inner resonators, *Wave Motion* 2015; 54:76–99.
- [7] Yang J., Lee J. S., Kim Y. Y., Metaporous layer to overcome the thickness constraint for broadband sound absorption, *J. Appl. Phys.* 2015; 117:174903.
- [8] Lagarrigue C., Groby J.-P., Dazel O., Tournat V., Design of metaporous supercells by genetic algorithm for absorption optimization on a wide frequency band, *Applied Acoustics* 2016; 102:49–54.
- [9] Xiong L., Nennig B., Aurégan Y., Bi W., Sound attenuation optimization using metaporous materials tuned on exceptional points, *J. Acoust. Soc. Am.* 2017; 142:2288–2297.
- [10] Yang J., Lee J. S., Kim Y. Y., Multiple slow waves in metaporous layers for broadband sound absorption, *J. Phys. D: Appl. Phys.* 2017; 50:015301.
- [11] Attenborough K., Macro- and micro-structure designs for porous sound absorbers, *Appl. Acoust.* 2019; 145:349–357.
- [12] Furstoss M., Thenail D., Galland M. A., Surface impedance control for sound absorption: direct and hybrid passive/active strategies, *J. Sound Vib.* 1997; 203:219–236.
- [13] Galland M.-A., Mazeaud B., Sellen N., Hybrid passive/active absorbers for flow ducts, *Appl. Acoust.* 2005; 66:691–708.
- [14] Batifol C., Zielinski T. G., Ichchou M. N., Galland M.-A., A finite-element study of a piezoelectric/poroelastic sound package concept, *Smart Mater. Struct.* 2007; 16:168–177.
- [15] Dupont J.-B., Galland M.-A., Active absorption to reduce the noise transmitted out of an enclosure, *Appl. Acoust.* 2009; 70:142–152.
- [16] Leroy P., Atalla N., Berry A., Herzog P., Three dimensional finite element modeling of smart foam, *J. Acoust. Soc. Am.* 2009; 126:2873–2885.
- [17] Zielinski T. G., Rak M., Acoustic absorption of foams coated with MR fluid under the influence of magnetic field, *J. Intell. Mater. Syst. Struct.* 2010; 21:125–131.
- [18] Zieliński T. G., Numerical investigation of active porous composites with enhanced acoustic absorption, *J. Sound Vib.* 2011; 330:5292–5308.
- [19] Betgen B., Galland M.-A., A new hybrid active/passive sound absorber with variable surface impedance, *Mech. Syst. Signal. Pr.* 2011; 25:1715–1726.
- [20] Zielinski T. G., Galland M.-A., Ichchou M. N., Fully-coupled finite-element modelling of active sandwich panels with poroelastic core, *J. Vib. Acoust.* 2012; 134:021007.
- [21] Johnson D. L., Koplik J., Dashen R., Theory of dynamic permeability and tortuosity in fluid-saturated porous media, *J. Fluid Mech.* 1987; 176:379–402.
- [22] Avellaneda M., Torquato S., Rigorous link between fluid permeability, electrical conductivity, and relaxation times for transport in porous media, *Phys. Fluids A* 1991; 3:2529–2540.
- [23] Champoux Y., Allard J.-F., Dynamic tortuosity and bulk modulus in air-saturated porous media, *J. Appl. Phys.* 1991; 70:1975–1979.
- [24] Pride S. R., Gangi A. F., Morgan F. D., Deriving the equations of motion for porous isotropic media, *J. Acoust. Soc. Am.* 1992; 92:3278–3290.
- [25] Pride S. R., Morgan F. D., Gangi A. F., Drag forces of porous-medium acoustics, *Phys. Rev. B* 1993; 47:4964–4978.
- [26] Lafarge D., Lemarinier P., Allard J. F., Tarnow V., Dynamic compressibility of air in porous structures at audible frequencies, *J. Acoust. Soc. Am.* 1997; 102:1995–2006.
- [27] Allard J. F., Atalla N., *Propagation of Sound in Porous Media: Modelling Sound Absorbing Materials*, Second Edition, Wiley, 2009.
- [28] Attenborough K., On the acoustic slow wave in air-filled granular media, *J. Acoust. Soc. Am.* 1987; 81:93–102.
- [29] Umnova O., Attenborough K., Li K. M., Cell model calculations of dynamic drag parameters in packings of spheres, *J. Acoust. Soc. Am.* 2000; 107:3113–3119.
- [30] Umnova O., Attenborough K., Li K. M., A cell model for the acoustical properties of packings of spheres, *Acta Acustica united with Acustica* 2001; 87:224–235.
- [31] Boutin C., Geindreau C., Estimates and bounds of dynamic permeability of granular media, *J. Acoust. Soc. Am.* 2008; 124:3576–3593.
- [32] Perrot C., Panneton R., Olly X., Periodic unit cell reconstruction of porous media: Application to open-cell aluminum foams, *J. Appl. Phys.* 2007; 101:113538.
- [33] Perrot C., Chevillotte F., Panneton R., Dynamic viscous permeability of an open-cell aluminum foam: Computations versus experiments, *J. Appl. Phys.* 2008; 103:024909.
- [34] Chevillotte F., Perrot C., Panneton R., Microstructure based model for sound absorption predictions of perforated closed-cell metallic foams, *J. Acoust. Soc. Am.* 2010; 128:1766–1776.
- [35] Zieliński T. G., Generation of random microstructures and prediction of sound velocity and absorption for open foams with spherical pores, *J. Acoust. Soc. Am.* 2015; 137:1790–1801.
- [36] Perrot C., Chevillotte F., Hoang M. T., Bonnet G., Bécot F.-X., Gautron L., Duval A., Microstructure, transport, and acoustic properties of open-cell foam samples: Experiments and three-dimensional numerical simulations, *J. Appl. Phys.* 2012; 111:014911.
- [37] Dautres O., Atalla N., Dong K., Effect of the microstructure closed pore content on the acoustic behavior of polyurethane foams, *J. Appl. Phys.* 2011; 110:064901.
- [38] Dautres O., Ouisse M., Atalla N., Ichchou M., Impact of the irregular micro-geometry of polyurethane foam on the macroscopic acoustic behavior predicted by a unit-cell model, *J. Acoust. Soc. Am.* 2014; 136:1666–1681.
- [39] Yang X. H., Ren S. W., Wang W. B., Liu X., Xin F. X., Lu T. J., A simplistic unit cell model for sound absorption of cellular foams with fully/semi-open cells, *Compos. Sci. Technol.* 2015; 118:276–283.
- [40] Park J. H., Minn K. S., Lee H. R., Yang S. H., Yu C. B., Pak S. Y., Oh C. S., Song Y. S., Kang Y. J., Youn J. R., Cell openness manipulation of low density polyurethane foam for efficient sound absorption, *J. Sound Vib.* 2017; 406:224–236.
- [41] Park J. H., Yang S. H., Lee H. R., Yu C. B., Pak S. Y., Oh C. S., Kang Y. J., Youn J. R., Optimization of low frequency sound absorption by cell size control and multiscale poroacoustics modeling, *J. Sound Vib.* 2017; 397:17–30.
- [42] Gao K., van Dommelen J. A. W., Geers M. G. D., Investigation of the effects of the microstructure on the sound absorption performance of polymer foams using a computational homogenization approach, *Eur. J. Mech. A. Solids* 2017; 61:330–344.
- [43] Chevillotte F., Perrot C., Guillon E., A direct link between microstructure and acoustical macro-behavior of real double porosity foams, *J. Acoust. Soc. Am.* 2013; 134:4681–4690.
- [44] Park J., Yang S. H., Minn K. S., Yu C. B., Pak S. Y., Song Y. S., Youn J. R., Design and numerical analysis of syntactic hybrid foam for superior sound absorption, *Mater. Des.* 2018; 142:212–220.
- [45] Zieliński T. G., Pore-size effects in sound absorbing foams with periodic microstructure: modelling and experimental verification using 3D printed specimens, in: Sas P., Moens D., van de Walle A. (Eds.), *Proceedings of ISMA2016 International Conference on Noise and Vibration Engineering and USD2016 International Conference on Uncertainty in Structural Dynamics*, 2016, p.95–104.
- [46] Gasser S., Paun F., Bréchet Y., Absorptive properties of rigid porous media: Application to face centered cubic sphere packing, *J. Acoust. Soc. Am.* 2005; 117:2090–2099.
- [47] Lee C.-Y., Leamy M. J., Nadler J. H., Acoustic absorption calculation in irreducible porous media: A unified computational approach, *J. Acoust. Soc. Am.* 2009; 126:1862–1870.
- [48] Zieliński T. G., Microstructure-based calculations and experimental results for sound absorbing porous layers of randomly packed rigid spherical beads, *J. Appl. Phys.* 2014; 116:034905.
- [49] Dung V. V., Panneton R., Gagné R., Prediction of effective properties and sound absorption of random close packings of monodisperse spherical particles: Multiscale approach, *J. Acoust. Soc. Am.* 2019; 145:3606–2624.
- [50] Perrot C., Chevillotte F., Panneton R., Bottom-up approach for microstructure optimization of sound absorbing materials, *J. Acoust. Soc. Am.* 2008; 124:940–948.

- [51] Meng H., Ao Q. B., Ren S. W., Xin F. X., Tang H. P., Lu T. J., Anisotropic acoustical properties of sintered fibrous metals, *Compos. Sci. Technol.* 2015; 107:10–17.
- [52] Meng H., Yang X. H., Ren S. W., Xin F. X., Lu T. J., Sound propagation in composite micro-tubes with surface-mounted fibrous roughness elements, *Compos. Sci. Technol.* 2016; 127:158–168.
- [53] Chen W., Chen T., Xin F., Wang X., Du X., Lu T. J., Modeling of sound absorption based on the fractal microstructures of porous fibrous metals, *Mater. Des.* 2016; 105:386–397.
- [54] Zieliński T. G., Microstructure representations for sound absorbing fibrous media: 3D and 2D multiscale modelling and experiments, *J. Sound Vib.* 2017; 409:112–130.
- [55] Ren S., Xin F., Lu T. J., Zhang C., A semi-analytical model for the influence of temperature on sound propagation in sintered metal fiber materials, *Mater. Des.* 2017; 134:513–522.
- [56] Ren S., Ao Q., Meng H., Xin F., Huang L., Zhang C., Lu T. J., A semi-analytical model for sound propagation in sintered fiber metals, *Composites Part B* 2017; 126:17–26.
- [57] Zieliński T. G., Chevillotte F., Deckers E., Sound absorption of plates with micro-slits backed with air cavities: Analytical estimations, numerical calculations and experimental validations, *Applied Acoustics* 2019; 146:261–279.
- [58] Opiela K. C., Rak M., Zieliński T. G., A concept demonstrator of adaptive sound absorber/insulator involving microstructure-based modelling and 3D-printing, in: Desmet W., Pluymers B., Moens D., Rottiers W. (Eds.), *Proceedings of ISMA2018 International Conference on Noise and Vibration Engineering and USD2018 International Conference on Uncertainty in Structural Dynamics*, 2018, p.1195–1207.
- [59] Stansbury J. W., Idacavage M. J., 3D printing with polymers: Challenges among expanding options and opportunities, *Dent. Mater.* 2016; 32:54–64.
- [60] Ngo T. D., Kashani A., Imbalzano G., Nguyen K. T., Hui D., Additive manufacturing (3D printing): A review of materials, methods, applications and challenges, *Composites Part B* 2018; 143:172–196.
- [61] Wang X., Jiang M., Zhou Z., Gou J., Hui D., 3D printing of polymer matrix composites: A review and prospective, *Composites Part B* 2017; 110:442–458.
- [62] Singh S., Ramakrishna S., Singh R., Material issues in additive manufacturing: A review, *J. Manuf. Processes* 2017; 25:185–200.
- [63] Zieliński T. G., Normalized inverse characterization of sound absorbing rigid porous media, *J. Acoust. Soc. Am.* 2015; 137:3232–3243.
- [64] ISO 10534-2: Determination of sound absorption coefficient and impedance in impedance tubes, 1998.
- [65] Zieliński T. G., Potoczek M., Śliwa R. E., Nowak Ł. J., Acoustic absorption of a new class of alumina foams with various high-porosity levels, *Arch. Acoust.* 2013; 38:495–502.
- [66] Attenborough K., Microstructures for lowering the quarter wavelength resonance frequency of a hard-backed rigid-porous layer, *Appl. Acoust.* 2018; 130:188–194.